Design of Deployable Soft Robots Through Plastic Deformation of Kirigami Structures

Audrey Sedal, Amirhossein H. Memar, Tianshu Liu, Yiğit Mengüç, and Nick Corson

***Abstract*—Kirigami-patterned mechanisms are an emergent class of deployable structure that are easy to fabricate and offer the potential to be integrated into deployable robots. In this letter, we propose a design methodology for robotic kirigami structures that takes into consideration the deformation, loading, and stiffness of the structure under typical use cases. We show how loading-deformation behavior of a kirigami structure can be mechanically programmed by imposing plastic deformation. We develop a model for plasticity in the stretching of a kirigami structure. We show the creation of kirigami structures that have an increased elastic region, and specified stiffness, in their deployed states. We demonstrate the benefits of such a plastically-deformed structure by integrating it into a soft deployable crawling robot: the kirigami structure matches the stiffness of the soft actuator such that the deployed, coupled behavior serves to mechanically program the gait step size.**

***Index Terms*—Soft robot materials and design, Kirigami.**

I. Introduction

DEPLOYABLE robots can transit from a compact form factor into an expanded shape better-suited for specific tasks or environments. This characteristic of deployability is useful for robots that need to be transported in a confined space (e.g. a space shuttle or underwater vehicle) before reaching their intended operating environment, or robots that need to pass through small spaces (e.g. a cave opening) before beginning an exploratory task.

A suitable deployable robot should be easy to fabricate, able to change function when it changes scale, and have a deployed shape that is well-suited to its intended usage. Therefore, designing for deployability requires careful consideration of the structural components involved. Rigid parts of the robot structure need to be integrated in a compact way, yet need to be arranged, connected and actuated so that a desired deployed shape is achievable. Some "tensegrity" designs mix rigid beams with tensile elastic components to achieve a desired deployment shape [1]–[3]. Other modules [4], [5] integrate rigid panel-like elements with flexible hinges; these are often termed "origami" robots. However, robots made with discrete, rigid components may have limited, and often complicated deployment schemes. Further, they often require fabrication of special components and high-effort assembly process.

One way to reduce the volumetric and kinematic limitations from rigid components is to replace them with soft pneumatic structures. Soft pneumatic structures are intrinsically deformable in their non-deployed state, meaning that they can be easily folded, pressed, or packed into compact configurations while retaining the ability to transform into their deployed shapes. The structures in [6] deploy through the inflation of truss-like pneumatic tubes, which become stiffer as air pressure increases. Easy fabrication and assembly is another key advantage of soft pneumatic structures in deployable robotics. The relatively simply constructed vine robot in [7] can deploy and operate in a variety of conditions, under a variety of environmental constraints. In [8], inflatable furniture and other static objects are fabricated by heat-sealing the flat cut sheets of inextensible thermoplastic polymer. In each of these examples, no advanced or especially precise fabrication is required, yet the devices achieve the specified deployed shapes. However, purely pneumatic soft structures have limitations in their deployed state. Such designs often require a minimum pressure to retain their deployed shape while functioning [6], resulting in a consistent power input requirement. Woven reinforcement materials, such as the meshes used in Meshworm [9] and CMMWorm [10], also offer tunable deformations constrained by the fibers in the mesh, but tuning the elastic recovery of such a structure without additional actuation is difficult due to fibers sliding against one another. Further, the motion of these robots in their deployed state is not necessarily easy to design or control: the deployable vine robot of [7] does not have a simple retraction scheme, and the tendon actuation of [6] limits the space of available motions.

Compared to other structures and materials that can achieve large-scale stretching and recovery, kirigami structures have two key advantages. They are easier to fabricate and offer the possibility for mechanical programming of their kinematics in the simple fabrication process. Kirigami-patterned mechanisms are easy to fabricate due to the fact that they can be cut on planar sheets of material, have mechanically programmable stiffness properties and offer the potential to be integrated into deployable robots. By patterning networks of thin cuts on a flat sheet, it is possible to change the kinematics of the sheet

Manuscript received September 9, 2019; accepted January 9, 2020. Date of publication February 3, 2020; date of current version February 17, 2020. This letter was recommended for publication by Associate Editor L. Wen and Editor K.-J. Cho upon evaluation of the reviewers' comments. This work was supported by Facebook Reality Labs. *(Corresponding author: Amirhossein H. Memar.)*

A. Sedal is with Facebook Reality Labs, Redmond, WA 98052 USA, and also with the Department of Mechanical Engineering, University of Michigan, Ann Arbor, MI 48109 USA (e-mail: asedal@umich.edu).

A. H. Memar, T. Liu, Y. Mengüç, and N. Corson are with Facebook Reality Labs, Redmond, WA 98052 USA (e-mail: ahajiagh@buffalo.edu; tianshu.liu@oculus.com; yigit.menguc@oregonstate.edu; nicholas.corson@fb.com).

This letter has supplementary downloadable material available at http://ieeexplore.ieee.org, provided by the authors.

Digital Object Identifier 10.1109/LRA.2020.2970943

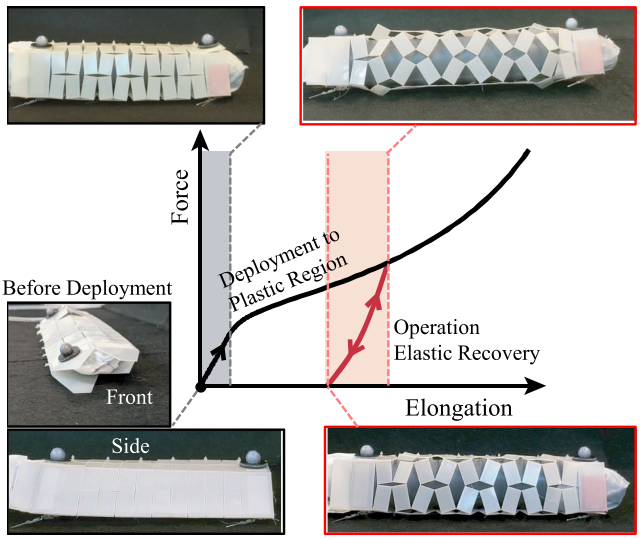

Fig. 1. Force-Elongation plot of kirigami structure: Elasto-plastic deployment region is shown in black, with corresponding robot photos outlined in black. Operating range is shown in red, with corresponding robot photos outlined in red.

material under loading and design a variety of behaviours. Kirigami-patterned structures are already an often-used basis for deployable static structure design, appearing in mechanisms and structures ranging from millimeter-scale [11], to architecture scale [12]. Further, kirigami patterns can be integrated with soft pneumatic actuation. Deformations of a kirigami structure can add function to a low-stiffness or low-impedance soft system.

In [13], various arrangements of buckled kirigami cuts are shown to produce linear and rotational actuation. Controlled buckling of a kirigami structure in [14] causes asymmetric friction that enables an extending actuator to crawl on rough surfaces. Because of their scalability, relatively easy fabrication, and design degrees of freedom, kirigami-based structures present a promising opportunity in the design of deployable robots.

Design of deployed states for kirigami structures has been well-investigated in the kinematic context [12], [15]. In contrast, loading properties of a kirigami structure require more characterization: while kirigami structures have been analyzed for their elastic stiffness [16], buckling response [17], and ultimate tensile strength [18], elasto-plastic deformation and loading have been neglected. Yet, plasticity occurs in a great variety of materials and has the potential to be leveraged in robotics. A plastically deformed robot structure has unique benefits: it can be kept in its deployed state without requiring a consistent power input, while elastic recovery in the deployed structure can accommodate external loads. To utilize the benefit of plasticity, a material with large range for plastic deformation and hardening needs to be chosen.

Loading-deformation behaviour of a robotic structure can be mechanically programmed by imposing plastic deformation. Depending on the initial cut dimensions and degree of plastic deformation undergone, the shape and size of the elastic recovery curve will change (Fig. 1), as will the resulting stiffness profile of

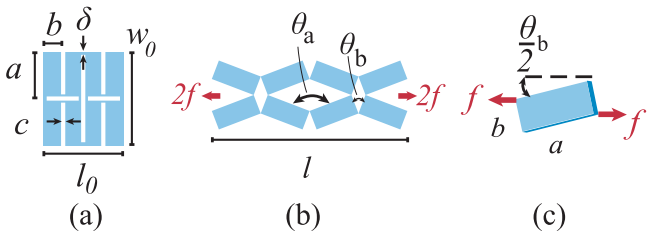

Fig. 2. Kirigami structure in initial (left) and deformed (right) states. This structure has 2 rows of n cuts of length a, and m cuts of length b. The distance between orthogonal cuts is δ, and the width of the cuts is c. Its initial width is w_0 and its initial length is l_0. When an axial force f is applied, the structure has length l and opening angles θ_a and θ_b as shown.

the structure. In the case of the strain-hardening material shown in Fig. 1, a cut structure can be loaded to a specific point, and then operates in its deployed state with a springback range wider than the initial elastic range of the robot.

In this letter, we propose a design methodology for robotic kirigami structures that takes use-case deformation, loading and stiffness into consideration from the beginning of the design process. We develop a model for plasticity in the stretching of a kirigami structure. Then, we describe a design methodology showing ways to leverage mechanical plasticity in a deployable robotics context. Specifically, we show the creation of kirigami structures that have an increased elastic region, and specified stiffness, in their deployed states. We demonstrate the benefits of such a plastically-deformed structure by integrating it into a soft, deployable crawling robot. We show how to design the deployed shape of the kirigami structure such that its corresponding springback characteristics matches the stiffness of the actuator to which it is attached. By better understanding the plastic loading properties of kirigami structures in robotic applications, we can create stronger designs with precise mechanical behaviour and known loading characteristics.

II. Plastic Kirigami Model and Validation

In this section, we perform a static analysis on the plastic deformation of a kirigami cut structure. The model presented below relies on three key assumptions: we assume that there is no buckling of the structure, no out-of-plane motion of the structure, and that the joints in the structure act as Euler-Bernoulli beams with no length change along their neutral axes.

A. Plastic Kirigami Model Description

In this letter, we consider kirigami structures with orthogonal patterned cuts for our modeling and experimentation. However, a similar approach can be applied to other types of cuts. The orthogonal patterned cuts on a sheet with length l_0 and width w_0 are shown in Fig. 2. The first cut family has 2 rows of n cuts of length a, and the second cut family has m cuts of length $2b$. The distance between orthogonal cuts is δ. To understand loading on the structure, we need to consider these kinematics alongside the elasticity and plasticity of the material. We can then consider the same sheet in a deformed configuration after a tensile force

f is applied to it (Fig. 2). The opening angle between two cuts segments of length a is θ_a. The opening angle between two cut segments of length b is $\theta_b = \pi - \theta_a$.

The kinematic relation between l in terms of a, b, and θ_b, derived in [15], is given by

$$\frac{l}{l_0} = \frac{a}{b}\cos\frac{\theta_b}{2} + \sin\frac{\theta_b}{2}. \tag{1}$$

In the deformed configuration, each rectangle of material in the sheet will have horizontal forces f on each of its corners (Fig. 2(c)). The total moment τ applied through joints on each of these 4 corners is balanced by the moment due to misalignment of the axial force f:

$$\tau = f\left[a\sin\left(\frac{\theta_b}{2}\right) - b\cos\left(\frac{\theta_b}{2}\right)\right]. \tag{2}$$

The bending moment M on each cut junction relates to the total moment τ by $\tau = 4M$. Yet, this moment M also depends on the properties of the joint in its bent state. To develop this relationship, we assume that the cut junctions act as elastic-plastic bending beams, where tensile stress is assumed to be small compared to bending stress. Each cut junction is considered as a beam with bending angle θ_a, radius of curvature ρ, height δ and thickness t, with coordinates x' and y' describing the location of a point on the cut beam's cross-section (Fig. 3). In [17], similar assumptions are made, but plasticity is neglected. For a structure in equilibrium, we can find that the moment is a function of both the kinematic properties and the beam stresses σ_{xx}. Then, we can use the following relationship to find M and the corresponding force on the structure f:

$$\begin{aligned} M &= \frac{f}{4}\left[a\sin\left(\frac{\theta_b}{2}\right) - b\cos\left(\frac{\theta_b}{2}\right)\right] \\ &= \int_{-\frac{t}{2}}^{\frac{t}{2}}\int_{-\frac{\delta}{2}}^{\frac{\delta}{2}} y'\sigma_{xx}(y,'\rho)dy'dx'. \end{aligned} \tag{3}$$

We develop the relationship between the sheet's material properties and its stress $\sigma_{x'x'}$ below by approximating the cut structure material as a bilinear isotropic hardening material [19]. The 1D constitutive equations for the stress σ, in terms of the Young's modulus E, elastic and plastic strains ε_{elast} and ε_{plast}, yield stress σ_{yield}, and hardening function (here, a constant) E_h are then

$$\sigma_{elast} = E\varepsilon_{elast} \tag{4}$$

for the elastic case. Stress σ_{plast} for a material in the plastic regime with linear isotropic hardening is written in terms of the plastic modulus E_h as

$$\sigma_{plast} = \sigma_{yield} + E_h(\varepsilon_{xx} - \varepsilon_{yield}). \tag{5}$$

Here, the plastic strain is the difference between the deformed strain and the yield strain: $\varepsilon_{plast} = \varepsilon - \varepsilon_{elast}$. Since the elastic regime of this material is linear, we can assume that

$$\sigma_{yield} = E\varepsilon_{yield}. \tag{6}$$

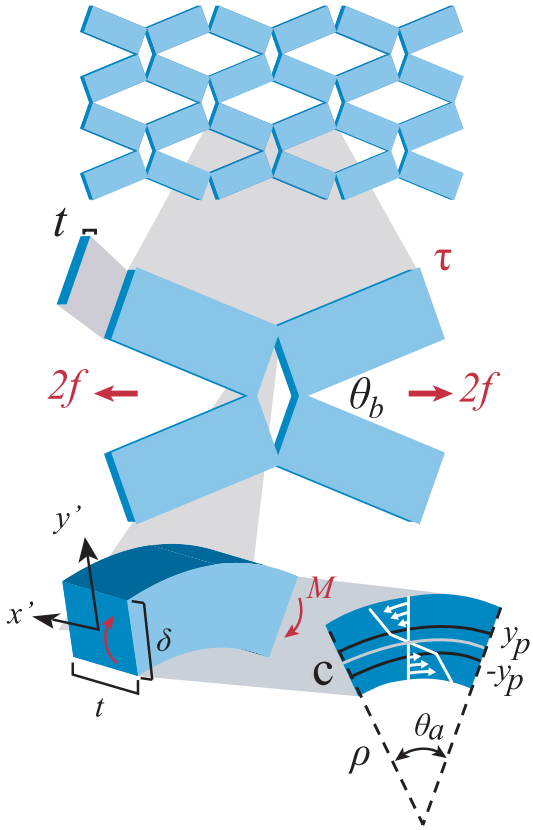

Fig. 3. Top: 2 adjacent kirigami structures as defined in Fig. 2 with $2n$ cuts of length a, m cuts of length b, force f applied in the x direction, and opening angles of $\theta_{a,b}$. Center: Kirigami repeating element, from the larger cut structure with moment τ on each corner. Bottom left: A cut junction of height δ and thickness t, with local coordinates x' and y'. Bottom right: cut view of the same cut junction with stresses shown by white arrows. For $|y'| < y_p$, the stresses are elastic. For $|y'| > y_p$, the stresses are plastic.

Assuming the central axis of the beam does not change length, the strain in the beam is given by

$$\varepsilon_{x'x'} = \frac{y'}{\rho}. \tag{7}$$

Initially, the moment M is fully elastic across the whole cross-sectional area A of the beam, giving

$$\begin{aligned} M(\rho) &= \iint_A y'\sigma_e(x,\rho)dA \\ &= \frac{E}{\rho}\int_{-\frac{t}{2}}^{\frac{t}{2}}\int_{-\frac{\delta}{2}}^{\frac{\delta}{2}} y'^2 dy'dx' \\ &= \frac{E}{\rho}\frac{\delta^3 t}{12}. \end{aligned} \tag{8}$$

However, parts of the beam cross-section yield as the curvature $1/\rho$ increases. We call y_p the cross-section coordinate in y' where the beam transitions from elastic to plastic deformation (Fig. 3). Since the neutral axis of the beam does not change length, the top part ($y' > y_p$) of the beam is in tensile plasticity, while the bottom ($y' < -y_p$) is in compressive plasticity. The

TABLE I
SET DESIGN PARAMETERS FOR VALIDATION SAMPLES

Sample no.	b (mm)	δ (mm)
1	7.367	0.305
2	3.556	0.305
3	1.078	0.305
4	7.367	0.406

general expression for $M(\rho)$ in (3) is then split about $\pm y_p$:

$$\begin{aligned} M(\rho) &= M_{elast}(\rho) + M_{plast}(\rho) \\ &= t\frac{E}{\rho}\int_{-y_p}^{y_p} y'^2 dy' \\ &\quad + 2t\int_{y_p}^{\frac{\delta}{2}} y'\left(\sigma_{yield} + E_h(\varepsilon_{xx} - \varepsilon_{yield})\right) dy'. \end{aligned} \quad (9)$$

We can find the value of y_p by setting $\sigma_{yield} = \sigma_{xx}(y_p)$ and using (4) and (7):

$$\sigma_{yield} = E\frac{y_p}{\rho}. \quad (10)$$

We assume that the beam bends as a circular segment, and that the cut kerf of the laser cutter c is 0.25 mm. This gives us ρ (shown in Fig. 3) as a function of θ_b as

$$\rho(\theta_b) = \frac{c}{\pi - \theta_b}. \quad (11)$$

Finally, we equate the expressions for $M(\rho)$ from (3) and (9), and isolate the force f as

$$f(\theta_b) = \frac{4M(\rho(\theta_b))}{a\sin\left(\frac{\theta_b}{2}\right) - b\cos\left(\frac{\theta_b}{2}\right)}. \quad (12)$$

The force f in (12) tends toward infinity as its denominator tends to zero. This model's singularity at $a\sin(\frac{\theta_b}{2}) - b\cos(\frac{\theta_b}{2}) = 0$ is equivalent to the kinematic locking equations shown in prior analysis [15].

Using the relationship between the axial force f on the structure, the kinematic parameter θ_b, and the cut pattern parameters a, b, δ and t, we can select parameters for kirigami structures that have specified loading-deformation relationships during plastic deformation.

B. Experimental Validation of Plasticity Model

To experimentally verify the plasticity model, we performed a tensile experiment on 4 sheets of varying design parameters b and δ. The kirigami pattern samples were cut from 0.178 mm (0.007 in) thickness sheets of BoPET (Mylar, DuPont-Teijin) using a CO2 laser cutter (Epilog Fusion M2). BoPET was chosen because of its known strain-hardening property [20] and compatibility with CO2 laser cutters. The values of design parameter chosen for each sample can be found in Table I. Common parameters for each sample were thickness $t = 0.178$ mm, cut length $a = 12.70$ mm, $n = 10$ and $m = 12$.

The kirigami sheet samples were tested on a tensile machine (Instron, 2350 load cell) using the ASTM standard tensile test method for plastics. We measured force f and axial elongation $l - l_0$.

TABLE II
MATERIAL PARAMETERS FIT FROM TENSILE EXPERIMENT

Parameter	Values (Pa)
E	7.343×10^8
σ_{yield}	1.045×10^7
E_h	5.801×10^7

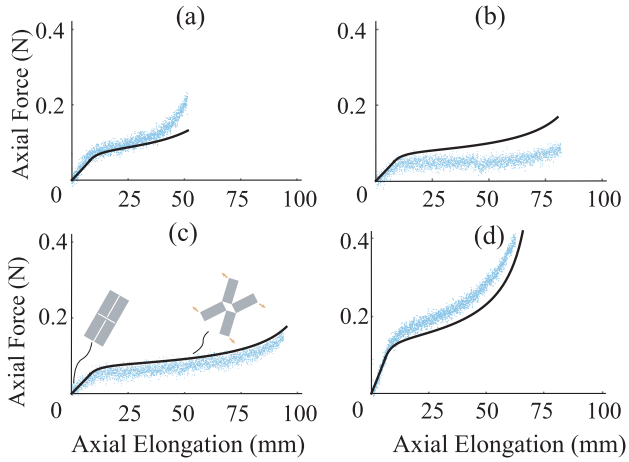

Fig. 4. Force-elongation measurements (points) and proposed model (lines) for the tested kirigami structure samples. (a) Sample 1, (b) Sample 2, (c) Sample 3, (d) Sample 4.

Following the tests, a parameter fit was performed on the recorded force-elongation data to estimate the Young's modulus E, yield stress σ_{yield}, and plastic modulus E_h. While these values are given on the Mylar data sheet, we also know that heating processes (such as the laser cutting process) have an effect on these parameters. For this reason, we fit E, σ_{yield} and E_h to our experimental data. The initial length l_0 of each structure was approximated as $l_0 = 2mb$. Then, using (1) and (12), we related the length changes $\Delta l = l - l_0$ to the measured axial force f. With this formulation for f, we used Wolfram Mathematica's implementation of Brent's principal axis algorithm to minimize the Root Mean Square Error (RMSE) between the result of the parameterized model expression and the measured extension-force pairs. For feasibility, the operating region of the deployed robot should not approach the kinematic singularity. So, for each design, whose elongation at the kinematic singularity is given by Δl_{lock}, we evaluated only force-elongation pairs where $\Delta l \leq 0.85\Delta l_{lock}$. Initial guess values for the material parameters were set as $E = 10^9$ Pa, $\sigma_{yield} = 10^7$ Pa, and $E_h = 10^8$ Pa, order-of magnitude guesses based on the Mylar datasheet plots. The fit values for material parameters E, σ_{yield}, and E_h are listed in Table II. The RMSE of force f for the fit was 3.72×10^{-2} N. Plots comparing the measurements to the force-elongation model with fitted parameters are shown in Fig. 4.

III. RELATIONSHIP BETWEEN ELASTO-PLASTIC PROPERTIES, OPERATING DIMENSIONS, AND STIFFNESS

Our design task is to choose the parameters a, b, n, m, t and δ for two benchmarks: (i) achieving an appropriate range of operating lengths Δl_{dep} due to elastic recovery of the structure

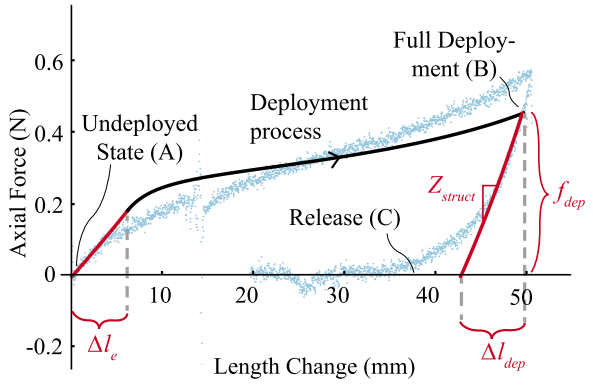

Fig. 5. Measured (points) and modeled (lines) force-elongation relationship of a plastically deformed kirigami structure with $a = 12.7$ mm, $b = 7.366$ mm, $n = 10$, $m = 12$, $t = 0.356$ mm and $\delta = 0.406$ mm, and the material properties E, σ_{yield}, and E_h as given in Table II.

after a deployment force f_{dep} is applied, and (ii) achieving a stiffness Z that matches or exceeds that of the actuator in its off-state. The force-elongation plot in Fig. 5 shows the deployment and operating regions of a sample kirigami structure obtained from both loading and unloading. This plot is used to describe the relationship between elasto-plastic properties, operating dimensions, and structure stiffness. This material and cut pattern are also used for the fabrication of the crawling robot of Section IV.

A. Deployed Length and Elastic Recovery

The desired length range in the structure's deployed state is determined by both the structure kinematics and the deployment force f_{dep}. We assume that $\delta << b$, and it is thus negligible when considering the gross deformation of the structure. In the initial compact configuration of the structure, $\theta_b = \pi$, and length $l_0 = 2mb$ (marked as point A on Fig. 5). Then, when we apply a force f_{dep}, the opening angle becomes $\theta_b = \theta_{dep}$, and the maximum deployed length $l = l_{dep}$: this configuration is marked by point B on Fig. 5. The deployment process is the transition between points A and B. We can determine deployment length l_{dep} and force f_{dep} in terms of θ_{dep} using (1) and (12) as

$$l_{dep} = 2\,m\left(a\cos\frac{\theta_{dep}}{2} + b\sin\frac{\theta_{dep}}{2}\right). \tag{13}$$

$$f_{dep} = \frac{4M(\rho(\theta_{dep}))}{a\sin\left(\frac{\theta_{dep}}{2}\right) - b\cos\left(\frac{\theta_{dep}}{2}\right)}. \tag{14}$$

The operating region is between points B and C on Fig. 5. Given a deployment force f_{dep}, we are interested in the estimation of length change in springback Δl_{dep}. Taking the deployed point B from Fig. 5 as a reference configuration, we consider the force $f_{op} \leq f_{dep}$ as the operational force that changes the opening angle from θ_{dep} to some $\theta_b \in [\theta_{dep}, \pi]$. This force is determined by (12), with a perturbation ΔM on the joint bending moment:

$$f_{op}(\theta_{dep}, \theta_b) = 4\frac{M(\theta_{dep}) + \Delta M(\theta_{dep}, \theta_b)}{a\sin\left(\frac{\theta_b}{2}\right) - b\cos\left(\frac{\theta_b}{2}\right)}, \tag{15}$$

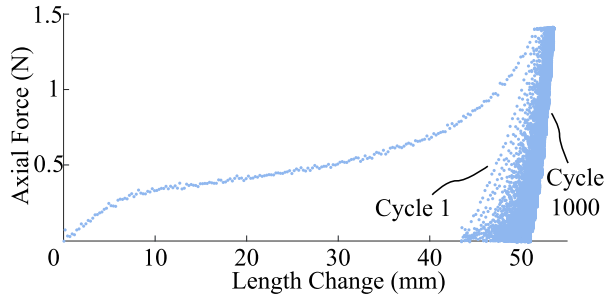

Fig. 6. Force-controlled cycle experiment on a kirigami structure with $a = 12.7$ mm, $b = 7.366$ mm, $n = 10$, $m = 12$, and $\delta = 0.406$ mm.

Since springback of the beam is purely elastic, we can then find $\Delta M(\theta_{dep}, \theta_b)$ based on (8):

$$\Delta M(\theta_{dep}, \theta_b) = E\frac{\delta^3 t}{12}\left[\frac{1}{\rho(\theta_{dep})} - \frac{1}{\rho(\theta_b)}\right]. \tag{16}$$

The length change in springback, Δl_{dep} is then the distance between l_{dep} and point C on Fig. 5. At point C, the axial force on the structure is zero. Solving (15) for $f_{op} = 0$ and replacing M from (9) gives the criterion for θ_0 for which $f = 0$:

$$\Delta M(\theta_{dep}, \theta_0) = -M(\theta_{dep}). \tag{17}$$

Obtaining θ_0 from (17), the solution for the operating length range Δl_{dep} is then

$$\Delta l_{dep}(\theta_{dep}, \theta_0) = l_{dep} - 2\,m\left(a\cos\frac{\theta_0}{2} + b\sin\frac{\theta_0}{2}\right). \tag{18}$$

B. Stiffness

Stiffness of the structure during operation is given by the slope Z (Fig. 5) of the operating region of the deployed kirigami structure. For simplicity, we approximate this region as linear. The simplified expression for the structure's springback stiffness is then

$$Z_{simplified} = \frac{f_{dep}}{\Delta l_{dep}}. \tag{19}$$

Design methodologies incorporating nonlinearity of the springback stiffness are left to future work.

C. Cycle Life

We characterized the cycle life of a kirigami structure. We performed 4 force-controlled cyclic tensile tests on kirigami samples with $a = 12.7$ mm, $b = 7.366$ mm, $n = 10$, $m = 12$, and $\delta = 0.406$ mm. The maximum force for each test was 0.4 N, 0.6 N, 0.8 N and 1.4 N respectively; all within the structure's plastic zone. The maximum velocity was 150 mm/min. In each case, the structure survived over 1000 cycles. Fig. 6 shows the force-elongation curve of the structure in the 1.4 N test. Some creep is noticeable: springback on the early cycles is larger than later cycles due to plastic hardening. The apparent springback impedance (slope) appears to increase as cycles continue. Yet, a limit cycle appears to be reached.

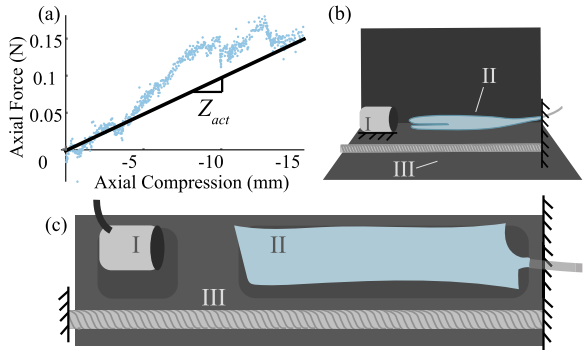

Fig. 7. Compressive actuator characterization. (a) Compression-Force plot of deflated everting actuator including data (points) and linear stiffness fit (line). (b) Schematic of side view of actuator characterization experiment. (c) Schematic of top view of actuator characterization experiment. In both (b) and (c), I refers to the force sensor (ATI Nano 17), II refers to the soft everting actuator, and III refers to the lead screw.

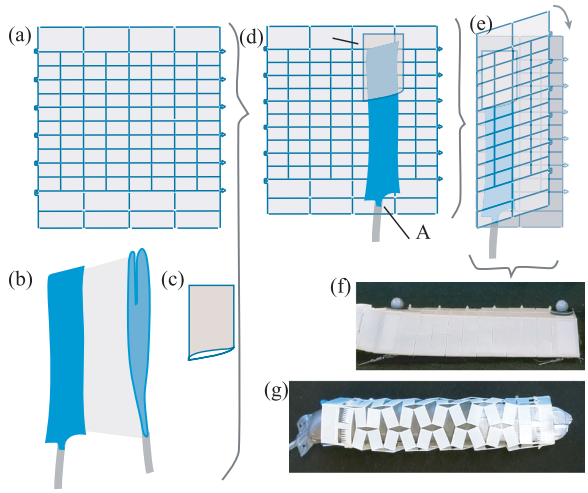

Fig. 8. Schematic of crawling robot components and assembly. (a) Laser-cut flat kirigami pattern. (b) Everting soft actuator (Left: top view. Right: side view.) (c) Nylon cap. (d) Actuator and cap placement on kirigami pattern. At point A, actuator base is taped to kirigami structure. At point B, fabric cap is taped to kirigami structre. Actuator end is then inserted into fabric cap without tape or glue. (e) Folding of kirigami pattern over cap and actuator. (f) Crawling robot in compact state with motion tracking markers. (g) Crawling robot after deployment (markers not shown).

IV. Implementation: Deployable Crawling Robot

In this section, we design a plastic kirigami structure to match stiffness with a pneumatic actuator, creating a soft deployable crawling robot. Deploying from a relatively flat compact state, the robot is small enough to slide through tight spaces. After deployment, the crawling robot benefits from a longer step length, and body retraction through springback of the plastically deformed structure.

A. Actuator Characterization

We chose a soft everting actuator [7] for integration because of its light weight, and inability to retract after pressure is applied. We made the actuator from heat-sealed polyurethane (Elastollan, BASF), and characterized its force in the operating pressure, as well as its off-state stiffness in recovery at atmospheric pressure. The soft everting actuator was placed in series with a force sensor (ATI Nano 17) and hold in place with a paper linear guide. It was inflated to 5 kPa, and then deflated back to atmospheric pressure. While at atmospheric pressure, a lead screw system was used to further compress the actuator by 15 mm to measure its off-state stiffness. This stiffness test was performed 3 times; data from one of the trials is shown in Fig. 7. Again approximating the actuator stiffness as linear, we fit a line to data from each of the 3 trials. The average measured stiffness of the actuator was $Z_{act} = 9.43$ N/m and the maximum force achieved by the actuator was 1.78 N. For effective integration with the kirigami structure, the off-state stiffness of the actuator should be less than or equal to the springback stiffness of the structure. In terms of (19):

$$Z_{act} \leq \frac{f_{dep}}{\Delta l_{dep}}. \tag{20}$$

B. Structure Design and Assembly

We constructed the crawler using a kirigami pattern with $a = 12.7$ mm, $b = 7.366$ mm, $n = 10$, $m = 12$, and $\delta = 0.406$ mm. We cut out 4 adjacent patterns with these parameters on a BoPET sheet of thickness $t = 0.356$ mm. We then folded the cut sheet into an enclosure (Fig. 8). We assumed that any unfolding during deployment did not result in bending forces on the kirigami sheet.

We heat sealed two sheets of thermoplastic urethane (BASF Elastollan, 0.11 mm sheet) at 145 °C to fabricate the actuator. The everting end was heat sealed closed, while a plastic tubing (1.57 mm inner diameter) was glued to the other end. The actuator's diameter was 19 mm. We sewed a fabric cap (Nylon, 70 Denier) and attached it to the front end of the kirigami enclosure to transmit actuator force to the kirigami structure. We coated the everting actuator with talc powder to reduce friction, and placed the folded actuator with its everting end inside the fabric cap. We attached the back end of the actuator and a small segment of the tubing to the back of the enclosure. Anisotropic friction was added to the bottom of the crawler by attaching angled pins to the kirigami structure. The crawler crawled over sheets of polyester felt.

C. Crawler Experiments

We performed two experiments on the crawler. In each, we initially deployed the crawler by raising the internal pressure to a specified value P_{dep}, using a pressure regulator (Festo VEAB). Then, we applied a cycle of amplitude P_{dep} to the actuator at 0.18 Hz for 120 seconds. We recorded the position of each end of the crawler at 100 Hz using an OptiTrack system with 2 cameras (Prime 17 W). Each marker was tracked from its initial location at the beginning of the experiment. A schematic of the experimental setup is given in Fig. 9. In the first experiment, P_{dep} was 4 kPa. In the second experiment, P_{dep} was 20 kPa. The first experiment is referred to as the "short step" experiment, while the second is the "long step" experiment.

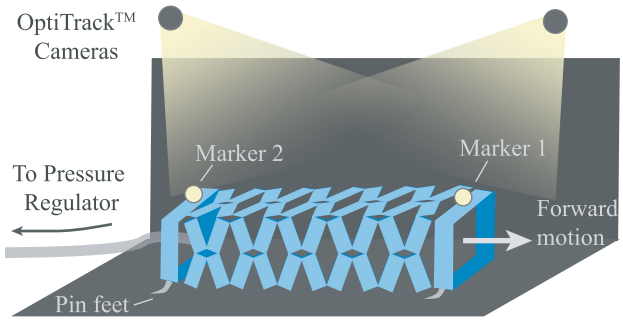

Fig. 9. Schematic of tracking experiment on crawler. Bent pins on the crawler base enable asymmetric friction on a felt surface. Markers and cameras track the motion of the crawler across the felt.

We evaluated the transmission loss of the system. For a deployment scenario with no transmission loss, the deployed opening angle θ_{dep} of the crawler structure along all 4 sides and all 4 corners would give us $F_{act,nl} = 8f(\theta_{dep})$ with f given in (14). The corresponding extension is then given by (7). For a given internal pressure and ideal cylinder-piston model and assuming the TPU wall does not stretch, we expect that the force at the tip of the actuator F_{act} is given by $F_{act,nl} = \pi(D/2)^2 P$, where $D = 19$ mm. However, there were transmission losses in converting input pressure to force and displacement due to the friction of the everting actuator with itself and the fabric cap. To evaluate the losses, we considered an effective diameter D_e that gives $F_{act,loss} = \pi(D_e/2)^2 P$. By performing a test where the actuator was inflated to 18 kPa, an effective diameter of $D_e = 11.6$ mm was estimated. This effective diameter was later used to predict the crawler's deformations and step sizes.

Further, we evaluated the performance of the plasticity model in the integrated crawler. Using the design specifications a, b, n, m, t and δ noted above, we used the plasticity model to predict the operating ranges, i.e. step sizes, Δl_{d1} and Δl_{d2}. Then, we measured the size of each step $\Delta l_{d1,n}$ and $\Delta l_{d2,n}$ for both experiments, as well as the permanent length change $l_{d,perm}$ in the long-step experiment.

D. Results

We recorded the motion of the crawler and related it to the plasticity model. In the short-step experiment, the crawler stayed in its elastic region, while in the long-step experiment it reached the plastic region during deployment. Fig. 10(a) and (b) show the measured motion of the crawler body for the first 60 seconds in the short- and long-step experiments, respectively. Specifically, we see the net positive (forward) motion of both markers while the motion of each marker in one pressure cycle are annotated. In the short-step experiment, actuator displaced a total of 2.46 mm. In the long-step experiment, the actuator displaced a total of 63.3 mm. Table III lists the modeled and average measured step sizes and permanent length changes for each experiment. Using these step sizes, and the corresponding modeled forces (maximum force of 0.12 N in the short step experiment, and 0.25 N in the long step experiment) we calculated the structure stiffness in the short-step experiment as 32.3 N/m per row of cuts (258.4 N/m overall for the 4-sided structure), and the structure

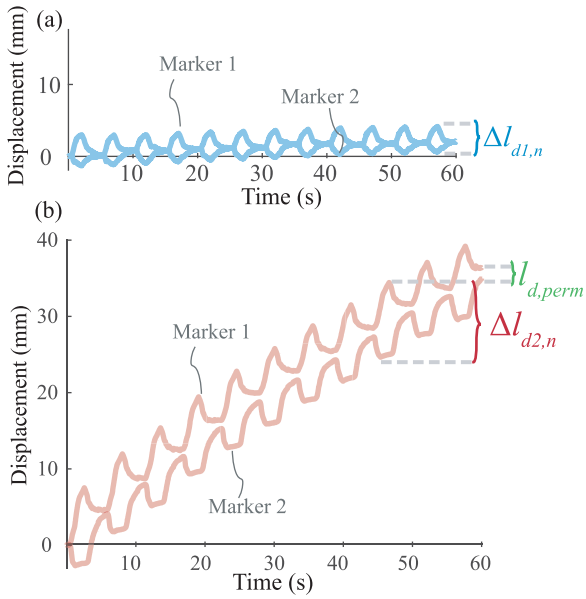

Fig. 10. Two deployment and operation experiments at different levels of deformation. (a) Position along the crawling robot's forward direction (Fig. 9) of the markers over time for the first 60 seconds of the short-step experiment. (b) Position along the crawling robot's forward direction (Fig. 9) of the markers over time for the first 60 seconds of the long-step experiment. In blue, the portion of the force-elongation curve corresponding to the short-step experiment, with step length Δl_{d1}. In red, the portion curve corresponding to the long-step experiment, with step length Δl_{d2}.

TABLE III
PREDICTED AND MEASURED STEP SIZES

		Experiment	
		Short Step (mm)	Long Step (mm)
Δl_{dep}	Predicted	3.88	9.60
	Meas. Mean (Std.)	3.80 (0.02)	8.00 (0.60)
$\Delta l_{dep,perm}$	Predicted	0.00	1.77
	Meas. Mean (Std.)	0.00(0.00)	1.09 (0.34)

stiffness in the long-step experiment as 33.4 N/m (267.2 N/m overall for the 4-sided cut structure).

V. DISCUSSION

We developed a model for plasticity in kirigami based on plastic deformation of Euler-Bernoulli beams, and validated it with a variety of samples with different design parameters. Fitting material properties gave results within the expected order of magnitude based on the data sheet of our chosen material. Agreement of these parameters is evidence that the plasticity model functions as intended: there do not appear to be additional hardening or softening phenomena in these structures that affect the parameter fits. The second, more important piece of evidence that the plasticity model functions as intended is agreement between model and experiment across all tested samples (RMSE $< 9.4\%$ N), and ability of the model to extrapolate using the same material parameters to a sample of higher thickness (Fig. 5).

Agreement enables use of the model in a soft, deployable crawling robot. We designed a kirigami structure whose stiffness during elastic recovery exceeded that of the soft everting actuator. When the actuator was cyclically pressurized between a set

point and atmospheric pressure, the robot took steps whose sizes were determined by both the deployment level and the pressure input at that specific cycles. Plastic deformation benefited the crawler: its step size was greater after deployment into the plastic region (the long-step experiment), compared to the short-step experiment where the crawler remained in its elastic region. Cycle life of the structure design used in the crawler exceeded 1000 cycles even at a larger maximum force (1.4 N in the cycle test vs. 0.25 N in the crawler prototype).

The key limitation of this approach is the irreversible nature of the deployment. After a kirigami structure has been plastically deformed, external forces are required to return it to its initial kinematic configuration. Then, it will no longer have the same loading behaviour that it had before plastic deformation. Though kirigami structures have a long cycle life within the deployed range, creep and out-of-range forces could significantly shorten the fatigue life of such a structure. Yet, relatively low expense and ease of manufacturing of kirigami structures make them suitable for single-use deployments followed by bounded repeating loads and deformations. A second limitation of our approach is that it assumes an absence of out-of-plane loading on the kirigami structures. The plasticity theory developed here can, however, be expanded to 3D kinematics and loading. Such an analysis would form the basis for exploring deployable kirigami robots with more complex 3D geometries: flat structures could deploy into complex 3D shapes. Further, the crawling robot presented here is a proof-of-concept prototype. This work can be expanded into the design and control of more sophisticated kirigami robots using different cut patterns than the orthogonal ones given here. One example is the rotating triangle pattern used for deployable shells by [12].

VI. Conclusion

Usually soft roboticists aim to avoid plastic deformation of parts in robot design. Yet, in materials that harden under strain, plastic deformation can be valuable tool in design and control. In this work, we propose a design method for soft robotic structures that leverages this plasticity. We show that in easy to fabricate, mechanically programmable kirigami structures, plastic strain hardening can enable deployability from an initially compact state to a larger functional volume, and can increase the range of elastic forces, and range of motion, and therefore work, feasible after deployment. Though this plastic model does not capture tensile behaviour of a kirigami structure near its kinematic singularity, it provides strong agreement (within 0.037 N) within the operating region, and provides the basis for the deformation-based design methodology shown in the following section.

The work presented here gives a theoretical and experimental basis for designing soft robots that leverage a fuller range of polymer properties by including plastic strain hardening. We have shown that plastic deformation of a kirigami structure can be used to create a deployable robot with no power draw in its deployed state. We have further shown how plasticity can be leveraged to selectively match stiffness to a soft actuator, enabling robot that is able to crawl uniquely because of these stiffness matches: the soft actuator lengthening the body, and elastic recovery (a.k.a. springback) of the kirigami structure contracting it again. This plasticity basis for soft robot design can be used in a variety of soft robotics applications.

Acknowledgment

The authors would like to thank Esther Foo, Heather Zager, and Mikhail Gordin for their help and support.

References

[1] H. Furuya, "Concept of deployable tensegrity structures in space application," *Int. J. Space Struct.*, vol. 7, no. 2, pp. 143–151, 1992.

[2] J. Panetta, M. Konaković-Luković, F. Isvoranu, E. Bouleau, and M. Pauly, "X-shells: A new class of deployable beam structures," *ACM Trans. Graph.*, vol. 38, no. 4, 2019, Art. no. 83.

[3] D. Zappetti, S. Mintchev, J. Shintake, and D. Floreano, "Bio-inspired tensegrity soft modular robots," in *Proc. Conf. Biomimetic Biohybrid Syst.*, 2017, pp. 497–508.

[4] K. Zhang and K. Althoefer, "Designing origami-adapted deployable modules for soft continuum arms," in *Proc. Annu. Conf. Towards Auton. Robot. Syst.*, 2019, pp. 138–147.

[5] Z. Zhakypov, C. H. Belke, and J. Paik, "Tribot: A deployable, self-righting and multi-locomotive origami robot," in *Proc. IEEE/RSJ Int. Conf. Intell. Robots Syst.*, 2017, pp. 5580–5586.

[6] S. Swaminathan, M. Rivera, R. Kang, Z. Luo, K. B. Ozutemiz, and S. E. Hudson, "Input, output and construction methods for custom fabrication of room-scale deployable pneumatic structures," in *Proc. ACM Interactive, Mobile, Wearable Ubiquitous Technologies*, vol. 3, no. 2, 2019, Art. no. 62.

[7] L. H. Blumenschein, L. T. Gan, J. A. Fan, A. M. Okamura, and E. W. Hawkes, "A tip-extending soft robot enables reconfigurable and deployable antennas," *IEEE Robot. Autom. Lett.*, vol. 3, no. 2, pp. 949–956, Apr. 2018.

[8] H. Sareen *et al.*, "Printflatables: printing human-scale, functional and dynamic inflatable objects," in *Proc. CHI Conf. Human Factors Comput. Syst.*, ACM, 2017, pp. 3669–3680.

[9] S. Seok, C. D. Onal, K.-J. Cho, R. J. Wood, D. Rus, and S. Kim, "Meshworm: A peristaltic soft robot with antagonistic nickel titanium coil actuators," *IEEE/ASME Trans. Mechatronics*, vol. 18, no. 5, pp. 1485–1497, Oct. 2013.

[10] A. D. Horchler *et al.*, "Worm-like robotic locomotion with a compliant modular mesh," in *Proc. Conf. Biomimetic Biohybrid Syst.*, 2015, pp. 26–37.

[11] W. Wang *et al.*, "Kirigami/origami-based soft deployable reflector for optical beam steering," *Adv. Functional Mater.*, vol. 27, no. 7, 2017, Art. no. 1604214.

[12] M. Konaković-Luković, J. Panetta, K. Crane, and M. Pauly, "Rapid deployment of curved surfaces via programmable auxetics," *ACM Trans. Graph.*, vol. 37, no. 4, 2018, Art. no. 106.

[13] M. A. Dias *et al.*, "Kirigami actuators," *Soft Matter*, vol. 13, no. 48, pp. 9087–9092, 2017.

[14] A. Rafsanjani, Y. Zhang, B. Liu, S. M. Rubinstein, and K. Bertoldi, "Kirigami skins make a simple soft actuator crawl," *Sci. Robot.*, vol. 3, no. 15, 2018, Art. no. eaar7555.

[15] Y. Tang and J. Yin, "Design of cut unit geometry in hierarchical kirigami-based auxetic metamaterials for high stretchability and compressibility," *Extreme Mechanics Lett.*, vol. 12, pp. 77–85, 2017.

[16] M. Isobe and K. Okumura, "Initial rigid response and softening transition of highly stretchable kirigami sheet materials," *Scientific Rep.*, vol. 6, 2016, Art. no. 24758.

[17] A. Rafsanjani and K. Bertoldi, "Buckling-induced kirigami," *Physical Rev. Lett.*, vol. 118, no. 8, 2017, Art. no. 084301.

[18] D.-G. Hwang and M. D. Bartlett, "Tunable mechanical metamaterials through hybrid kirigami structures," *Scientific Rep.*, vol. 8, no. 1, 2018, Art. no. 3378.

[19] R. Hill, *The Mathematical Theory of Plasticity*. London, U.K.: Oxford Univ. Press, 1998, vol. 11.

[20] D.-T. Films, *Mylar Polyester Film, Product Information*. 222367D datasheet, 2019.